# Cardiac Fiber Unfolding by Semidefinite Programming

Hongying Li*, Marc C. Robini, *Member, IEEE*, Feng Yang, Isabelle Magnin, and Yuemin Zhu

***Abstract*—Diffusion-tensor imaging allows noninvasive assessment of the myocardial fiber architecture, which is fundamental in understanding the mechanics of the heart. In this context, tractography techniques are often used for representing and visualizing cardiac fibers, but their output is only qualitative. We introduce here a new framework toward a more quantitative description of the cardiac fiber architecture from tractography results. The proposed approach consists in taking three-dimensional (3-D) fiber tracts as inputs, and then unfolding these fibers in the Euclidean plane under local isometry constraints using semidefinite programming. The solution of the unfolding problem takes the form of a Gram matrix which defines the two-dimensional (2-D) embedding of the fibers and whose spectrum provides quantitative information on their organization. Experiments on synthetic and real data show that unfolding makes it easier to observe and to study the cardiac fiber architecture. Our conclusion is that 2-D embedding of cardiac fibers is a promising approach to supplement 3-D rendering for understanding the functioning of the heart.**

***Index Terms*—Cardiac imaging, diffusion-tensor imaging, dimensionality reduction, semidefinite programming, tractography.**

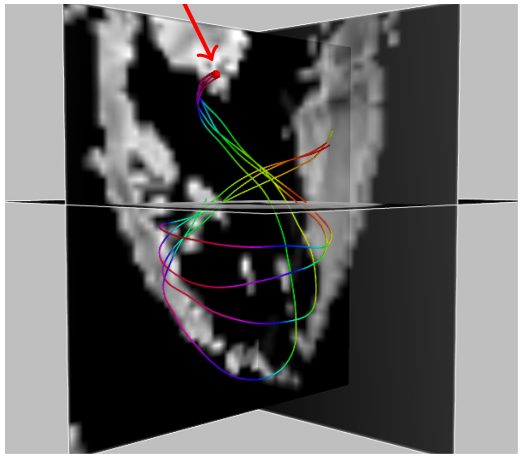

Fig. 1. Fiber tracts obtained from human cardiac DTI data (superimposed on the B0 volume). The tracts are located in the left ventricle and pass through the voxel pointed by the red arrow.

## I. Introduction

THE human myocardium is composed of branched myocytes which are approximately 25 $\mu$m in diameter and 100 $\mu$m in length, and which are attached to each other by intercalated disks. Therefore, contrary to brain white matter tissue, the myocardium does not contain so-called "fibers" at the microscopic scale. However, cardiac myocytes form elongated structures with a preferential local orientation, which are often regarded as fibers (or bundles of fibers) at coarse scales. The notion of cardiac fibers has been used since the end of the 19th century to study the structure of the myocardium [1]–[11], and cardiac fiber organization is fundamental in understanding the functioning of the heart [12], [13]. More recently, the existence of fiber patterns in the myocardium has been further confirmed by diffusion-tensor imaging (DTI) [14]; this technique measures water diffusion in the myocardium region and allows noninvasive assessment of the human myocardial architecture [15]–[21]. In cardiac DTI, tractography produces a set of three-dimensional (3-D) curves which represent the paths followed by myocardial fibers, thereby facilitating the high-level perception of the fiber architecture of the heart (the fibers are usually interpreted visually from 3-D rendering with a coloring scheme based on curve features such as local tangent directions [22]).

The helical pattern of cardiac fibers can be successfully reconstructed from DTI tractography results [23], [24], but tractography is usually regarded as the final stage in representing the cardiac fiber architecture. In fact, up to now, few studies have focused on the quantitative description of fiber tracts, whether cardiac or neuronal. In [25], a clustering methodology was proposed to find correspondences across a fiber population obtained from cardiac DTI data. In [26] and [27], the authors used computational techniques to quantify and compare the shape of fibers in the human brain. Finally, clustering approaches to classifying white matter fiber bundles were reported in [28] and [29].

We present here a framework for unfolding cardiac fibers in order to facilitate the description of their architecture. Our approach consists in taking 3-D fiber tracts as inputs, unfolding them in the Euclidean plane, and extracting quantitative parameters from the resulting two-dimensional (2-D) embedding. This new type of representation makes it easier to observe the relative positions of the fibers and allows a more accurate assessment of their organization. To motivate our idea, Fig. 1 displays four cardiac fiber tracts with the B0 volume in the background. These fibers pass through a same point, but even though they are few, their organization is difficult to apprehend.

Manuscript received April 13, 2014; revised August 8, 2014; accepted September 18, 2014. Date of publication September 29, 2014; date of current version January 16, 2015. This work was supported by the French ANR under ANR-13-MONU-0009-01. *Asterisk indicates corresponding author.*

*H. Li is with the CREATIS, 69621 Villeurbanne cedex, France (e-mail: lihongying17@gmail.com).

M. C. Robini, I. Magnin, and Y. Zhu are with the CREATIS, 69621 Villeurbanne cedex, France (e-mail: marc.robini@creatis.insa-lyon.fr; isabelle.magnin@creatis.insa-lyon.fr; zhu@creatis.insa-lyon.fr).

F. Yang is with the Department of Biomedical Engineering, Beijing JiaoTong University, 100044 Beijing, China (e-mail: feng.yang@bjtu.edu.cn).

Color versions of one or more of the figures in this paper are available online at http://ieeexplore.ieee.org.

Digital Object Identifier 10.1109/TBME.2014.2360797

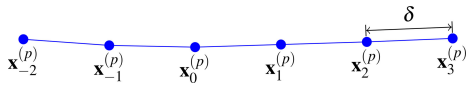


Fig. 2. Fiber tract $\mathbf{X}^{(p)} = (\mathbf{x}_{-m_p}^{(p)}, \ldots, \mathbf{x}_{0}^{(p)}, \ldots, \mathbf{x}_{n_p}^{(p)})$ is represented by a finite sequence of points. The distance between two adjacent points is a constant $\delta$ called the step-length.

We propose to unfold the fiber tracts using a nonlinear dimensionality reduction technique (see [30], [31] for an overview)—namely, semidefinite embedding [32]—which positions data points as far apart as possible under local distance constraints. More precisely, each fiber is sampled at regular intervals, and the resulting points are placed in the Euclidean plane by maximizing the sum of the squared distances between pairs of points connected in a fiber-isometry graph. This graph is constructed to reflect likely similarities between neighboring fibers, and the optimization is performed by semidefinite programming (SDP). The solution of the SDP problem takes the form of a Gram matrix from which the embedded fibers are obtained by diagonalization, and whose spectrum provides quantitative information on fiber organization. In particular, the ratio of the second to the third largest eigenvalues measures the closeness of the 3-D input fibers to a 2-D manifold, and the ratio of the second to the first largest eigenvalues measures the dispersion of the fibers within the embedding. This leads to the definition of two quantitative indices on fiber organization: *embedding accuracy* (EA) and *fiber dispersion* (FD).

This paper is organized as follows. In Section II, we describe the methodology of unfolding, which includes the representation of fibers, the definition of suitable distance and neighborhoods for isometry constraints, and the formulation in terms of SDP. Section III is devoted to experimental results on synthetic data and real human cardiac data. A brief discussion and concluding remarks are given in Section IV.

## II. Methodology

### A. Fiber Representation

Fibers are represented by finite sequences of points, as shown in Fig. 2. Given an ordering of the fibers, we denote the $p$th fiber by

$$\mathbf{X}^{(\mathrm{p})} = \left(\mathbf{x}_{-\mathrm{m_p}}^{(\mathrm{p})}, \ldots, \mathbf{x}_{0}^{(\mathrm{p})}, \ldots, \mathbf{x}_{\mathrm{n_p}}^{(\mathrm{p})}\right) \tag{1}$$

where $m_p$ and $n_p$ are positive integers, and $\mathbf{x}_0^{(p)}$ is called the *reference point* of the fiber. The set of all fiber points is

$$\mathbf{X} = \bigcup_{p=1}^{P} \bigcup_{i=-m_p}^{n_p} \{\mathbf{x}_i^{(p)}\} \tag{2}$$

where $P$ is the number of fibers. We let $N$ denote the total number of points in $\mathbf{X}$, that is,

$$N = \sum_{p=1}^{P} (m_p + n_p + 1). \tag{3}$$

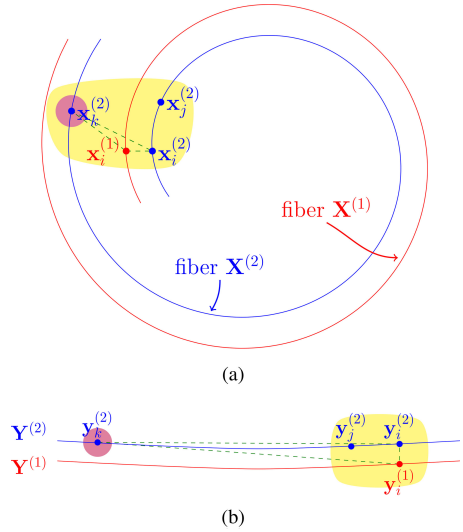


Fig. 3. Spiral-shaped fibers before and after unfolding: (a) fiber points in the yellow region are close to each other in the sense of the Euclidean distance in space; (b) in the embedding, the image point $\mathbf{y}_k^{(2)}$ of $\mathbf{x}_k^{(2)}$ is distant from the other image points.

The distance between two adjacent points $\mathbf{x}_i^{(p)}$ and $\mathbf{x}_{i+1}^{(p)}$ in a same fiber $\mathbf{X}^{(p)}$ is a constant $\delta > 0$ which we call the *step-length*.

For simplicity, we will sometimes drop the superscript indicating the fiber number. In this case, a point $\mathbf{x}_i^{(p)}$ is denoted by $\mathbf{x}_m$ with

$$m = \begin{cases} i + m_p + 1, & \text{if } p = 1 \\ i + m_p + p + \sum_{j=1}^{p-1} (m_j + n_j), & \text{if } p > 1. \end{cases} \tag{4}$$

In other words, $(\mathbf{x}_1, \ldots, \mathbf{x}_N)$ is the ordering of the set of all fiber points obtained by concatenating $\mathbf{X}^{(1)}, \ldots, \mathbf{X}^{(P)}$.

### B. Fiber Isometry

A map $f$ from a metric space $(E, d_E)$ to another metric space $(F, d_F)$ is called an isometry if $d_F(f(a), f(b)) = d_E(a, b)$ for all $(a, b) \in E^2$. To extend the notion of isometry to fibers points, we must give a meaning to distance preservation for a one-to-one correspondence between the set of fiber points $\mathbf{X} \subset \mathbb{R}^3$ and an embedding $\mathbf{Y} = \{\mathbf{y}_1, \ldots, \mathbf{y}_N\}$ of $\mathbf{X}$ in the Euclidean plane. To do so, we equip $\mathbf{Y}$ with the standard Euclidean norm (which we simply denote by $\|\cdot\|$), and we define a distance function $d_{\mathbf{X}}$ on $\mathbf{X}$ that reflects our knowledge about cardiac fiber organization (see Section II-D). In particular, $d_{\mathbf{X}}$ should discriminate pairs of nearby points in a same fiber from pairs of nearby points in different fibers. This is illustrated in Fig. 3. The four points in the yellow region in Fig. 3(a) are close in terms of the Euclidean distance in space, but in the embedding, the image point $\mathbf{y}_k^{(2)}$ of $\mathbf{x}_k^{(2)}$ is distant from the other three image points; so in terms of $d_{\mathbf{X}}$, the fiber points $\mathbf{x}_i^{(1)}$, $\mathbf{x}_i^{(2)}$ and $\mathbf{x}_j^{(2)}$ should be close to each other and distant from $\mathbf{x}_k^{(2)}$.

### C. Fiber Unfolding

Given a set $\{\mathbf{X}^{(1)}, \ldots, \mathbf{X}^{(P)}\}$ of sequential cardiac fibers in $\mathbb{R}^3$, unfolding embeds the $\mathbf{X}^{(p)}$'s in the Euclidean plane to supplement the description of their organization. The one-to-one correspondence between the set of fiber points $\mathbf{X}$ and its embedding $\mathbf{Y}$ is obtained by "stretching" the fibers (that is, by maximizing the sum of the squared distances between pairs of points) while preserving neighborhood relationships defined in terms of $d_{\mathbf{X}}$. Formally, the optimization problem is the following:

$$\begin{aligned} &\text{maximize} \sum_{m,n=1}^{N} \|\mathbf{y}_m - \mathbf{y}_n\|^2 \\ &\text{subject to } a_{mn}\|\mathbf{y}_m - \mathbf{y}_n\| = a_{mn}\|\mathbf{x}_m - \mathbf{x}_n\| \end{aligned} \tag{5}$$

where the $a_{mn}$'s are the binary coefficients of an adjacency matrix $\mathbf{A}$ designed to preserve fiber features such as arc-length along a same fiber and isometry between adjacent fibers. The construction of $\mathbf{A}$ is detailed in Section II-E; it involves the distance $d_{\mathbf{X}}$ defined below.

### D. Distance Between Fiber Points

The definition of $d_{\mathbf{X}}$ is not straightforward because 3-D cardiac fibers have a somewhat spiral shape. In a nutshell, the distance we propose moves two fiber points away if they do not belong to a same local fiber-bundle region. By way of illustration, referring back to Fig. 3, the idea is to put a large distance between $\mathbf{x}_k^{(2)}$ and the three other fiber points.

The natural distance between two points $\mathbf{x}_i^{(p)}$ and $\mathbf{x}_j^{(p)}$ in a same fiber $\mathbf{X}^{(p)}$ is the fiber-length between them; so we let $d_{\mathbf{X}}(\mathbf{x}_i^{(p)}, \mathbf{x}_j^{(p)})$ be the length of a polygonal chain approximating $\mathbf{X}^{(p)}$ between these two points:

$$d_{\mathbf{X}}(\mathbf{x}_i^{(p)}, \mathbf{x}_j^{(p)}) = |j-i|\delta \tag{6}$$

for all $p \in \{1, \ldots, P\}$ and all $i, j \in \{-m_p, \ldots, n_p\}$. If $\mathbf{x}_i^{(p)}$ and $\mathbf{x}_j^{(q)}$ do not belong to a same fiber, we extend this definition by setting

$$d_{\mathbf{X}}(\mathbf{x}_i^{(p)}, \mathbf{x}_j^{(q)}) = \sqrt{\left(|j-i|\delta\right)^2 + \left(d_{i,j}^{(p,q)}\right)^2} \tag{7}$$

where $|j-i|\delta$ is to be interpreted here as the arc-length between the local fiber-bundle regions containing $\mathbf{x}_i^{(p)}$ and $\mathbf{x}_j^{(q)}$, and where $d_{i,j}^{(p,q)}$ is the mean distance between the $p$th and $q$th fibers at points $i$ and $j$, that is,

$$d_{i,j}^{(p,q)} = \frac{1}{2}\left(\|\mathbf{x}_i^{(p)} - \mathbf{x}_i^{(q)}\| + \|\mathbf{x}_j^{(p)} - \mathbf{x}_j^{(q)}\|\right). \tag{8}$$

It should be stressed that $d_{\mathbf{X}}$ is not the Euclidean distance between two points (except for successive points in a same fiber) and that it depends on the choice of the reference points $x_0^{(1)}, \ldots, x_0^{(P)}$. This distance has intuitive appeal if the reference points are located in a small region of interest which we call the *reference region*.

### E. Construction of the Adjacency Matrix

The purpose of the $N \times N$ adjacency matrix $\mathbf{A} = [a_{m,n}]$ is to relax the distance constraints that are not tied to cardiac fiber organization. The coefficients of $\mathbf{A}$ are defined by

$$a_{mn} = \begin{cases} 1, & \text{if } \mathbf{x}_n \in \mathcal{N}_k(\mathbf{x}_m) \text{ and } \mathbf{x}_m \in \mathcal{N}_k(\mathbf{x}_n) \\ 0, & \text{otherwise} \end{cases} \tag{9}$$

where $\{\mathcal{N}_k(\mathbf{x}_1), \ldots, \mathcal{N}_k(\mathbf{x}_N)\}$ is a collection of structural neighborhoods which can be interpreted as local fiber bundle regions, and where the integer $k \geqslant 3$ is a size parameter which fixes the number of points in the neighborhoods and thus controls local isometry. If $k$ is set to its minimum value (that is, $k = 3$), the distance constraints between pairs of points in different fibers are relaxed, and hence the original local structure is lost in the unfolding process. Increasing $k$ reinforces the distance constraints and widens their range, which makes it harder to flatten the original 3-D structure. In the present study, the value of $k$ is chosen so that the neighborhoods involve three to six fibers (more details are given in the experimental and discussion sections).

The neighborhoods $\mathcal{N}_k(\mathbf{x}_m)$ are constructed in the following three steps:

1) For every fiber point $\mathbf{x}_i^{(p)}$, we let $\mathcal{S}(\mathbf{x}_i^{(p)})$ be the set of fiber points whose elements are
   a) $\mathbf{x}_i^{(p)}$ and its nearest neighbors $\mathbf{x}_{i-1}^{(p)}$ and $\mathbf{x}_{i+1}^{(p)}$ in the $p$th fiber (it being understood that there is only one nearest neighbor if $i = -m_p$ or $n_p$)
   b) the three nearest neighbors of $\mathbf{x}_i^{(p)}$ with respect to $d_{\mathbf{X}}$ in each fiber $\mathbf{X}^{(q)}$ ($q \neq p$), that is, the fiber points $\mathbf{x}_{i_1}^{(q)}$, $\mathbf{x}_{i_2}^{(q)}$ and $\mathbf{x}_{i_3}^{(q)}$ such that

$$\begin{aligned} &\max_{j\in\{1,2,3\}} d_{\mathbf{X}}\left(\mathbf{x}_i^{(p)}, \mathbf{x}_{i_j}^{(q)}\right) \\ &< \min_{\mathbf{x}\in\mathbf{X}^{(q)}\setminus\left\{\mathbf{x}_{i_1}^{(q)}, \mathbf{x}_{i_2}^{(q)}, \mathbf{x}_{i_3}^{(q)}\right\}} d_{\mathbf{X}}(\mathbf{x}_i^{(p)}, \mathbf{x}). \end{aligned} \tag{10}$$

   Therefore, $\mathcal{S}(\mathbf{x}_i^{(p)})$ contains either $3P-1$ or $3P$ fiber points depending on whether $\mathbf{x}_i^{(p)}$ is a fiber extremity or not.
2) Since $\mathbf{S} = \{\mathcal{S}(\mathbf{x}_1), \ldots, \mathcal{S}(\mathbf{x}_N)\}$ is not symmetric in the sense that $\mathbf{x}_n \in \mathcal{S}(\mathbf{x}_m)$ does not necessarily imply that $\mathbf{x}_m \in \mathcal{S}(\mathbf{x}_n)$, we introduce the symmetrization $\{\mathcal{S}^\dagger(\mathbf{x}_1), \ldots, \mathcal{S}^\dagger(\mathbf{x}_N)\}$ of $\mathbf{S}$ defined by

$$\mathcal{S}^\dagger(\mathbf{x}_m) = \mathcal{S}(\mathbf{x}_m) \cup \{\mathbf{x}_n \in \mathbf{X} \mid \mathbf{x}_m \in \mathcal{S}(\mathbf{x}_n)\} \tag{11}$$

   for all $m \in \{1, \ldots, N\}$.
3) Finally, we adjust the range of the local isometry constraints by restricting the symmetrization of $\mathbf{S}$ to neighborhoods of size at most $k+1$. More precisely, if $\mathcal{S}^\dagger(\mathbf{x}_m)$ has more than $k+1$ elements, we define the structural neighborhood $\mathcal{N}_k$ of $\mathbf{x}_m$ to be the union of $\mathbf{x}_m$ with its $k$ nearest neighbors in $\mathcal{S}^\dagger(\mathbf{x}_m)$ with respect to $d_{\mathbf{X}}$:

$$\mathcal{N}_k(\mathbf{x}_m) = \{\mathbf{x}_m\} \cup \{\mathbf{x}_{m,1}, \ldots, \mathbf{x}_{m,k}\} \tag{12}$$

where $\mathbf{x}_{m,1}, \ldots, \mathbf{x}_{m,k} \in \mathcal{S}^{\dagger}(\mathbf{x}_m) \setminus \{\mathbf{x}_m\}$ are such that

$$\max_{l \in \{1,\ldots,k\}} d_{\mathbf{X}}(\mathbf{x}_m, \mathbf{x}_{m,l}) < \min_{\mathbf{x} \in \mathcal{S}^{\dagger}(\mathbf{x}_m) \setminus \mathcal{N}_k(\mathbf{x}_m)} d_{\mathbf{X}}(\mathbf{x}_m, \mathbf{x}). \quad (13)$$

If $\mathcal{S}^{\dagger}(\mathbf{x}_m)$ has no more than $k+1$ elements, then we simply set $\mathcal{N}_k(\mathbf{x}_m) = \mathcal{S}^{\dagger}(\mathbf{x}_m)$.

### *F. Solving the Unfolding Problem by SDP*

Given a set $\mathbf{Y} = \{\mathbf{y}_1, \ldots, \mathbf{y}_N\}$ of points in the Euclidean plane, we let $\mathbf{G} = [g_{mn}]$ be the Gram matrix of $\mathbf{Y}$; that is, $g_{mn} = \mathbf{y}_m \cdot \mathbf{y}_n$ (the standard inner product of $\mathbf{y}_m$ and $\mathbf{y}_n$) for every $(m,n) \in \{1,\ldots,N\}^2$. Then, since $\|\mathbf{y}_m - \mathbf{y}_n\|^2 = g_{mm} - 2g_{mn} + g_{nn}$, the constraints of the unfolding problem (5) are equivalent to

$$a_{mn}(g_{mm} - 2g_{mn} + g_{nn}) = a_{mn}\|\mathbf{x}_m - \mathbf{x}_n\|^2. \quad (14)$$

The unfolding problem has a translational degree of freedom: if $\{\mathbf{y}_1^*, \ldots, \mathbf{y}_N^*\}$ is a solution, then so is $\{\mathbf{y}_1^* + \mathbf{a}, \ldots, \mathbf{y}_N^* + \mathbf{a}\}$ for any 2-D point $\mathbf{a}$. To obtain a single solution, we add the constraint that $\mathbf{Y}$ be centered on the origin, that is, $\sum_n \mathbf{y}_n = \mathbf{0}$, or equivalently,

$$\sum_{m,n} g_{mn} = 0 \quad (15)$$

(this equivalence follows from the fact that $\|\sum_n \mathbf{y}_n\|^2 = \sum_{m,n} \mathbf{y}_m \cdot \mathbf{y}_n$). The constraint (15) also allows to express the objective function of the unfolding problem in terms of the trace of $\mathbf{G}$:

$$\sum_{m,n} \|\mathbf{y}_m - \mathbf{y}_n\|^2 = \sum_{m,n}(g_{mm} - 2g_{mn} + g_{nn}) = 2N\sum_m g_{mm} = 2N\mathrm{tr}(\mathbf{G}). \quad (16)$$

In the end, since a matrix is Gramian if and only if it is positive semidefinite, the unfolding problem is equivalent to the following SDP problem:

$$\text{maximize } \mathrm{tr}(\mathbf{G}) \text{ subject to } \begin{cases} \mathbf{G} \text{ is symmetric positive semidefinite} \\ \sum_{m,n} g_{mn} = 0 \\ a_{mn}(g_{mm} - 2g_{mn} + g_{nn}) = a_{mn}\|\mathbf{x}_m - \mathbf{x}_n\|^2. \end{cases} \quad (17)$$

(We refer to [33] for a comprehensive introduction to SDP and to [35] for the SDP solver used in our experiments.)

The question that remains is how to compute a solution $\mathbf{Y}^* = \{\mathbf{y}_1^*, \ldots, \mathbf{y}_N^*\}$ to the original unfolding problem from a solution $\mathbf{G}^*$ to (17). Since $\mathbf{G}^*$ is symmetric, it can be written in the form $\mathbf{G}^* = \mathbf{P}\mathbf{\Lambda}\mathbf{P}^T$, where $\mathbf{\Lambda} = \mathrm{diag}\{\lambda_1, \ldots, \lambda_N\}$ is the diagonal matrix whose entries are the eigenvalues of $\mathbf{G}^*$, and $\mathbf{P} = [\mathbf{v}_1 \ \ldots \ \mathbf{v}_N]$ is the orthogonal matrix whose columns are the eigenvectors of $\mathbf{G}^*$ associated with $\lambda_1, \ldots, \lambda_N$. The eigenvalues $\lambda_n$ are nonnegative (because $\mathbf{G}^*$ is positive semidefinite), and we assume that they are arranged in decreasing order: $\lambda_1 \geqslant \cdots \geqslant \lambda_N \geqslant 0$. The coefficients $g_{mn}^*$ of $\mathbf{G}^*$ are given by

$$g_{mn}^* = \sum_{k=1}^{N} \lambda_k \mathbf{v}_{k,m} \mathbf{v}_{k,n} \quad (18)$$

where $\mathbf{v}_{k,n}$ denotes the $n$th component of $\mathbf{v}_k$. Equivalently, $\mathbf{G}^*$ is the Gram matrix of the vectors $\boldsymbol{\psi}_1, \ldots, \boldsymbol{\psi}_N$ defined by

$$\boldsymbol{\psi}_n = (\sqrt{\lambda_1}\mathbf{v}_{1,n}, \ldots, \sqrt{\lambda_N}\mathbf{v}_{N,n}). \quad (19)$$

If the fibers $\mathbf{X}^{(1)}, \ldots, \mathbf{X}^{(p)}$ lie near a 2-D manifold, then $\lambda_2 \gg \lambda_3$ [32], and thus

$$\boldsymbol{\psi}_n \approx (\sqrt{\lambda_1}\mathbf{v}_{1,n}, \sqrt{\lambda_2}\mathbf{v}_{2,n}, 0 \ldots, 0). \quad (20)$$

Hence, the solution $\mathbf{Y}^*$ to the original unfolding problem is obtained by truncating the vectors $\boldsymbol{\psi}_n$ to their first two components; that is, we set

$$\mathbf{y}_n^* = (\sqrt{\lambda_1}\mathbf{v}_{1,n}, \sqrt{\lambda_2}\mathbf{v}_{2,n}) \quad (21)$$

for all $n \in \{1, \ldots, N\}$.

The ratio $\lambda_3/\lambda_2$ can be used to measure the accuracy of approximation (20) (the smaller $\lambda_3/\lambda_2$, the closer the original set of 3-D fibers to a 2-D manifold), and $\lambda_2/\lambda_1$ measures the dispersion of the fibers within the 2-D embedding. Since these two ratios are in the interval $[0,1]$, we can use them to express EA and FD as percentages:

$$\text{EA } (\%) = 100(1 - \lambda_3/\lambda_2) \quad (22)$$

$$\text{FD } (\%) = 100\,\lambda_2/\lambda_1. \quad (23)$$

### *G. Distance Measure Between Two Embeddings*

We conclude our methodological description with the definition of a distance measure between embeddings of a same set of fibers $\mathbf{X}$. This measure is denoted by $d$ and used in our experiments below. Given two embeddings $\mathbf{Y} = (\mathbf{y}_1, \ldots, \mathbf{y}_N)$ and $\mathbf{Z} = (\mathbf{z}_1, \ldots, \mathbf{z}_N)$ of $\mathbf{X}$, we define

$$d(\mathbf{Y}, \mathbf{Z}) = \frac{1}{N^2} \sum_{m \neq n} d_{m,n}(\mathbf{Y}, \mathbf{Z}) \quad (24)$$

where $d_{m,n}(\mathbf{Y}, \mathbf{Z})$ is the absolute difference of the distances between the $m$th and $n$th points in $\mathbf{Y}$ and $\mathbf{Z}$:

$$d_{m,n}(\mathbf{Y}, \mathbf{Z}) = \big|\|\mathbf{y}_m - \mathbf{y}_n\| - \|\mathbf{z}_m - \mathbf{z}_n\|\big|. \quad (25)$$

## III. Experiments

### *A. Synthetic Examples*

*1) Equidistant Helical Fibers:* We first test our unfolding algorithm on the four equidistant helical fibers displayed in Fig. 4; this choice is motivated by the helical ventricular myocardial band model [23]. Each fiber is represented by 100 points and has a length of 49 (the unit of measurement is arbitrary, but we can think in terms of millimeters). The distance between two nearby fibers is 0.93. Fig. 5 shows the embedding produced by our unfolding algorithm with $k = 9$. Note that the horizontal and vertical axis scales are the same, as for all the embeddings displayed in this paper. The embedding reveals the structure of the 3-D curves: It consists of parallel segments with length

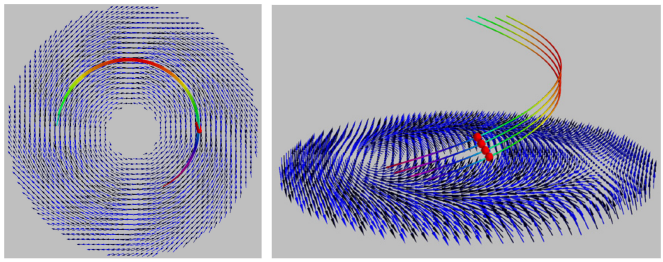


Fig. 4. Equidistant helical fibers. Each fiber has a length of 49 (arbitrary unit), the distance between two adjacent fibers is 0.93, and the red points are the reference points.

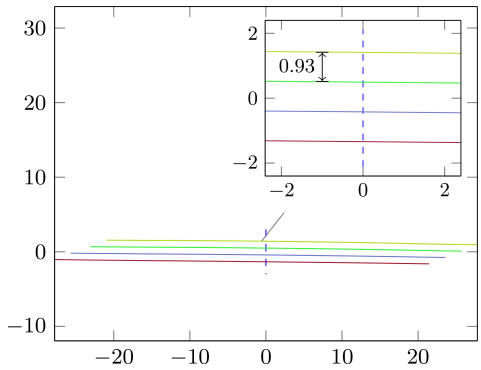


Fig. 5. Embedding of the equidistant helical fibers obtained with $k = 9$. The length and relative positions of the helixes are preserved.

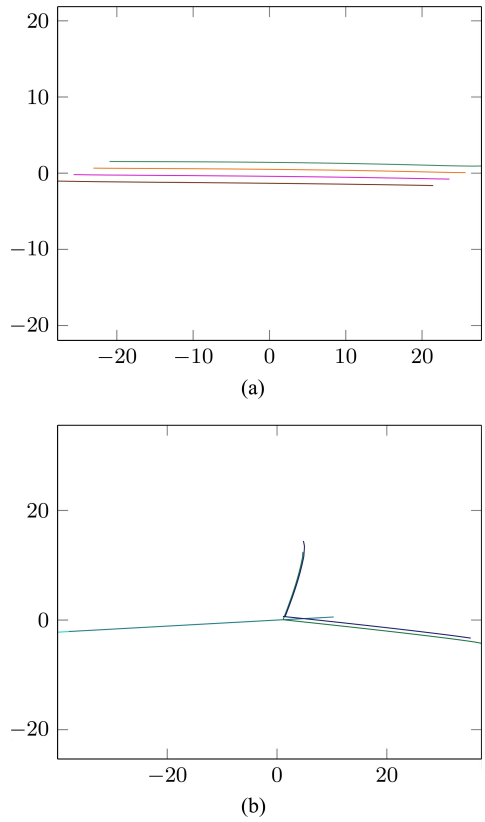


Fig. 6. Embeddings of the equidistant helical fibers obtained with (a) $k = 11$ and (b) $k = 5$.

equal to that of the helixes, and the distance from one segment to the next is also the same as that between the helixes. These observations are supplemented by the three largest normalized eigenvalues of the Gram matrix $\mathbf{G}^*$ solution to (17): $\lambda_1 = 0.9950$, $\lambda_2 = 4.7 \times 10^{-3}$, and $\lambda_3 = 10^{-4}$. Following definitions (22) and (23), the EA is 97.8%, which indicates that the helixes are very close to a 2-D manifold, and the FD within the embedding is smaller than 0.5%, which is in agreement with the fact that the helixes are equidistant and close to each other.

A guideline for choosing the neighborhood-size parameter $k$ is that it should be about three times the number of fibers that defines the range of the local isometry constraints. So $k$ ranges from 3 to $3P$ if there are $P$ fibers to unfold, and setting $k = 3Q$ with $Q \in \{1, \ldots, P\}$ means that each structural neighborhood $\mathcal{N}_k(\mathbf{x}_m)$ contains points in about $Q$ different fibers (the exact number depends on the fiber extremities in the considered neighborhood). Back to our example, for the value $k = 9$ considered above, most neighborhoods $\mathcal{N}_9(\mathbf{x}_m)$ contain ten points distributed in three neighboring fibers; in other words, the range of the local isometry constraints is limited to three fibers, which is sufficient since the helixes are equidistant. The unfolding results remain similar for values of $k$ larger than 9, but they deteriorate when the structural neighborhoods involve less than nine points in three different fibers (that is, when $k \leqslant 7$). This is illustrated in Fig. 6, which shows the embeddings obtained with $k = 11$ and $k = 5$.

*2) Fanning and Highly Curled Fibers:* We consider here the set of fanning fibers shown in Fig. 7(a) and the set of highly curled fibers shown in Fig. 7(b). Each set contains a total of 800 points distributed among seven fibers. The elevation angle is constant along every fiber and varies from one fiber to the other, ranging from $-45^\circ$ to $45^\circ$ with a $15^\circ$ step-angle for the fanning fibers, and from $0^\circ$ to $30^\circ$ with a $5^\circ$ step-angle for the curled fibers.

Fig. 8 displays the embeddings obtained by our unfolding algorithm with $k = 15$ and using the reference points at the locations pointed by the arrows in Fig. 7. Let us first examine the embedding of the fanning fibers in Fig. 8(a). The unfolded fibers are straight line segments revealing the fanning structure of the original 3-D fibers. The EA is almost perfect (99.6%) because the 3-D fibers lie on a cylinder, and the important FD within the embedding is confirmed by its quantitative measurement (40.6%). Furthermore, the angle $\alpha$ between every pair of nearby line segments is about $15.1^\circ$, and the angle $\beta$ between the outer line segments is about $90.7^\circ$; that is, we recover almost exactly the step and the range of the elevation angle that were used to generate the 3-D fibers. The embedding of the curled fibers [see Fig. 8(b)] consists of nearly straight lines. The associated accuracy is 94.9%, the FD is only 6.3%, and the step and range angles $\alpha$ and $\beta$ are close to the step and the range of the elevation angle in the 3-D fibers (but not as close as for the fanning fibers). This slight decrease in accuracy compared to the fanning

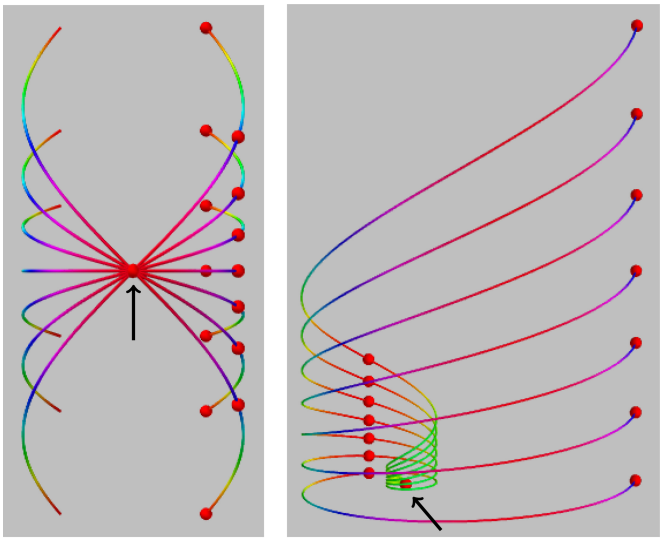

(a) (b)

Fig. 7. Synthetic sets of fanning and curled fibers, both with three groups of reference points. The first group consists of reference points at the same location (pointed by the arrow), and the other two groups are vertically aligned.

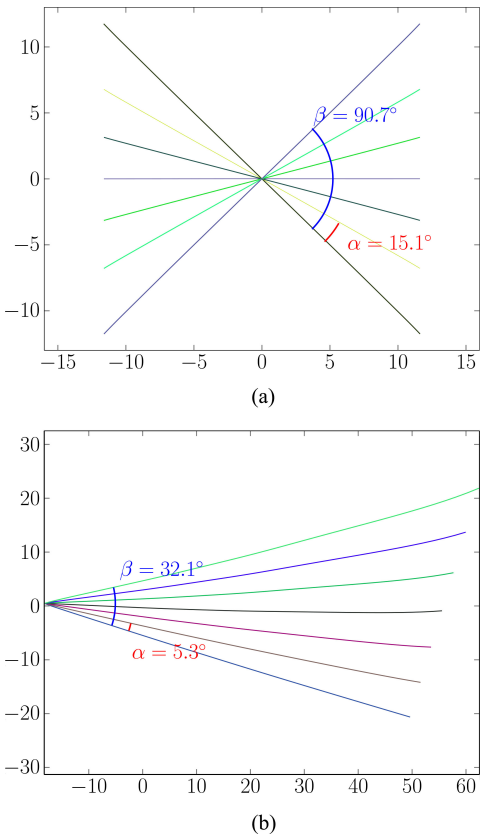


(a) (b)

Fig. 8. Embeddings of the sets of fibers shown in Fig. 7: (a) fanning fibers; (b) curled fibers. (In both cases, we used $k = 15$ and the reference points pointed by the arrows.)

TABLE I
LARGEST NORMALIZED EIGENVALUES, EA, AND FD OF THE UNFOLDED FANNING FIBERS FOR INCREASING VALUES OF $k$

| | $\lambda_1$ | $\lambda_2$ | $\lambda_3$ | EA (%) | FD (%) |
|---|---|---|---|---|---|
| $k = 6$ | 1.0000 | 0.0000 | 0.0000 | - | - |
| $k = 9$ | 0.7134 | 0.2857 | 0.0004 | 99.8 | 40.0 |
| $k = 12$ | 0.7141 | 0.2833 | 0.0018 | 99.3 | 39.6 |
| $k = 15$ | 0.7099 | 0.2886 | 0.0010 | 99.6 | 40.6 |
| $k = 18$ | 0.7053 | 0.2897 | 0.0035 | 98.8 | 41.0 |
| $k = 21$ | 0.7027 | 0.2912 | 0.0038 | 98.7 | 41.4 |

TABLE II
STEP AND RANGE ANGLES OF THE UNFOLDED FANNING FIBERS FOR INCREASING VALUES OF $k \geqslant 9$

| | $\alpha$ | $\beta$ |
|---|---|---|
| $k = 9$ | 14.9 | 89.4 |
| $k = 12$ | 14.9 | 89.4 |
| $k = 15$ | 15.1 | 90.7 |
| $k = 18$ | 15.2 | 91.4 |
| $k = 21$ | 15.3 | 92.2 |

TABLE III
LARGEST NORMALIZED EIGENVALUES, EA, AND FD OF THE CURLED FIBERS FOR INCREASING VALUES OF $k$

| | $\lambda_1$ | $\lambda_2$ | $\lambda_3$ | EA (%) | FD (%) |
|---|---|---|---|---|---|
| $k = 6$ | 1.0000 | 0.0000 | 0.0000 | - | - |
| $k = 9$ | 1.0000 | 0.0000 | 0.0000 | - | - |
| $k = 12$ | 0.9352 | 0.0587 | 0.0043 | 92.6 | 6.2 |
| $k = 15$ | 0.9363 | 0.0590 | 0.0030 | 94.9 | 6.3 |
| $k = 18$ | 0.9394 | 0.0578 | 0.0015 | 97.4 | 6.1 |
| $k = 21$ | 0.9357 | 0.0591 | 0.0034 | 94.2 | 6.3 |

fibers is due to the more complex, spiral-shaped structure of the underlying 2-D manifold. The small FD reflects the fact that the curled fibers move slowly away from each other.

To assess the effect of the neighborhood-size parameter $k$, we repeated the above unfolding experiments with $k \in \{6, 9, 12, 18, 21\}$ (recall that we used $k = 15$ previously). In the case of the fanning fibers, the original fiber structure is lost when $k = 6$ (the structural neighborhoods $\mathcal{N}_k(\mathbf{x}_m)$ contain too few points to keep the unfolded fibers grouped together), but the other embeddings are visually the same: the distance $d$ [see (24)] between any two embeddings obtained for $k \geqslant 9$ is smaller than 0.13, a value to be compared to the average length of the 3-D fibers (about 40). Quantitatively, Table I shows that for $k \geqslant 9$, the spectrum of the Gram matrix is approximately constant, and hence so are the EA and the FD. Moreover, the step and range angles given in Table II are very close to $15°$ and $90°$. So the distribution of the original elevation angle is preserved by the unfolding process. As regards the curled fibers, the original structure is lost when $k \leqslant 9$, but the embeddings obtained for $k \geqslant 12$ are similar, as Table III shows—the distance $d$ between any two such embeddings is smaller than 0.36, to be compared with an average fiber length of about 60. The step and range angles given in Table IV confirm that the distribution of

TABLE IV
STEP AND RANGE ANGLES OF THE UNFOLDED CURLED FIBERS FOR INCREASING VALUES OF $k \geqslant 12$

| | $\alpha$ | $\beta$ |
|---|---|---|
| $k = 12$ | 5.2 | 31.2 |
| $k = 15$ | 5.3 | 31.9 |
| $k = 18$ | 5.4 | 32.1 |
| $k = 21$ | 5.4 | 32.1 |

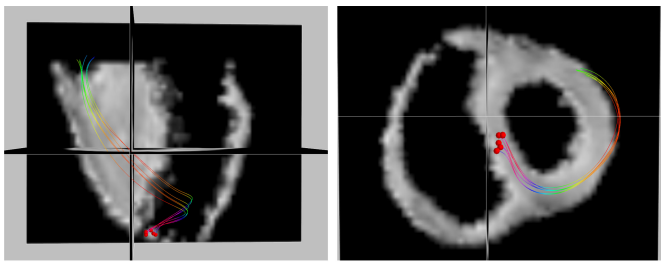

(a) (b)

Fig. 9. Simple configuration consisting of six cardiac fibers close to one another (long- and short-axis views).

the original elevation angle is preserved by unfolding when the neighborhood size is large enough.

We finally repeated all the previous experiments on the fanning and curled fibers using the other two groups of reference points (that is, the sets of vertically aligned points shown in Fig. 7). We did not observe any difference with the results obtained when using the overlapping reference points, which leads to the conclusion that our unfolding algorithm is not sensitive to the choice of the reference region. However, when dealing with real data, it is practically (and intuitively) better to choose a reference region as small as possible.

### B. Unfolding Real Cardiac Fibers

Our real data consist of diffusion-weighted images of *ex vivo* human hearts acquired with a Siemens 1.5 T Magnetom Avanto using the following settings: TE $= 98$ ms, TR $= 8600$ ms, FOV $= 256 \times 256$ mm$^2$, slice thickness $= 2$ mm, number of slices $= 52$, slice size $= 128 \times 128$, diffusion sensitivity $= 10^3$ s $\times$ mm$^{-2}$, and 12 gradient directions. The acquisition sequence is a 2-D EPI diffusion-weighted sequence with a twice-refocused diffusion preparation.

The cardiac fibers considered here are selected from fiber sets obtained with the probabilistic tractography method proposed in [34]. Unless stated otherwise, these fibers are discretized with a step-length of half the voxel size (they contain about 160 points on average), and the neighborhood-size parameter $k$ is set to 15 (so according to our discussion in Section III-A, most structural neighborhoods involve five different fibers).

*1) Simple Fiber Configuration:* We start with the simple configuration shown in Fig. 9, which consists of six cardiac fibers that are close to each other along their whole lengths. Figs. 10(b), (d) and (f) show the corresponding embeddings obtained when moving the reference region from one extremity

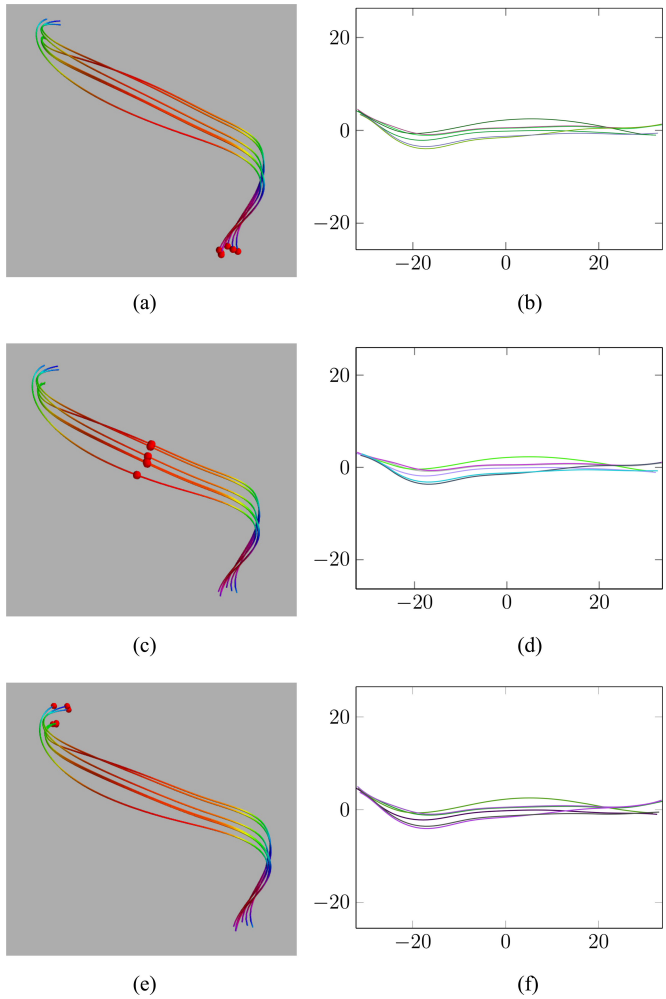


(a) (b) (c) (d) (e) (f)

Fig. 10. Embeddings of the fibers in Fig. 9 obtained with different sets of reference points: (b), (d) and (f) are the embeddings associated with the reference point locations displayed in red in (a), (c) and (e), respectively. (Axis units are mm.)

TABLE V
LARGEST NORMALIZED EIGENVALUES, EA, AND FD OF THE EMBEDDINGS SHOWN IN FIG. 10

| Reference region | $\lambda_1$ | $\lambda_2$ | $\lambda_3$ | EA (%) | FD (%) |
|---|---|---|---|---|---|
| Lower [see Fig. 10(b)] | 0.9907 | 0.0064 | 0.0008 | 87.5 | 0.64 |
| Middle [see Fig. 10(d)] | 0.9896 | 0.0073 | 0.0010 | 86.3 | 0.73 |
| Higher [see Fig. 10(f)] | 0.9906 | 0.0070 | 0.0007 | 90 | 0.70 |

to the other. We observe that the unfolded fibers remain close to each other (similar to the 3-D fibers) and that the unfolding algorithm is not sensitive to moving the reference region. This is further confirmed by measuring the distance $d$ between any two of the three embeddings: The result remains smaller than 0.25% of the average length of the 3-D fibers. The largest normalized eigenvalues of the Gram matrices associated with the three embeddings are reported in Table V. The EA is high enough to conclude that the 3-D fibers lie near a 2-D manifold,

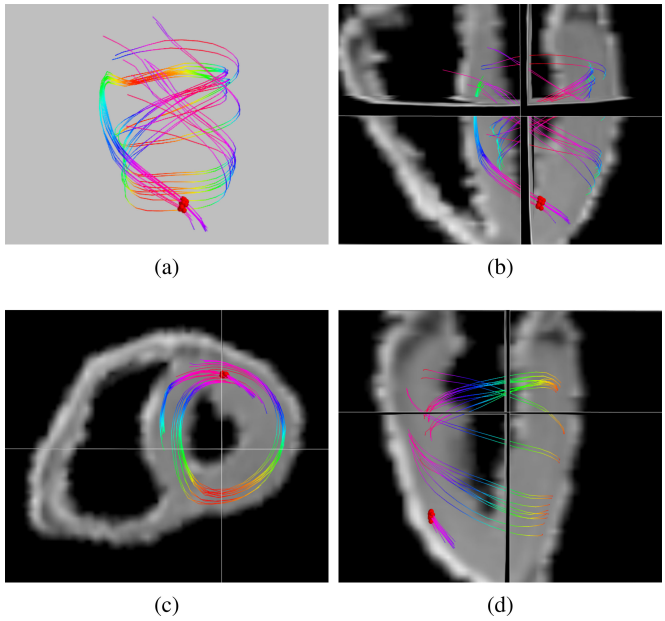


Fig. 11. Thirteen cardiac fibers with organization subject to misinterpretation. (The red points are the reference points used for unfolding.)

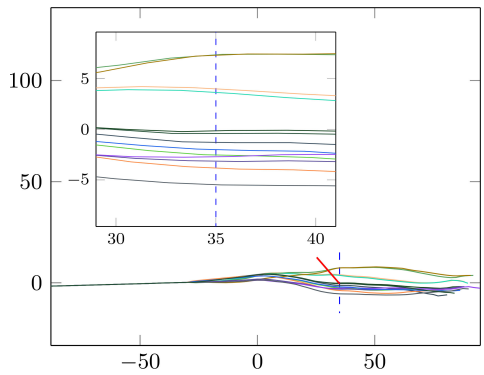


Fig. 12. Embedding of the fibers shown in Fig. 11. (Axis units are mm.)

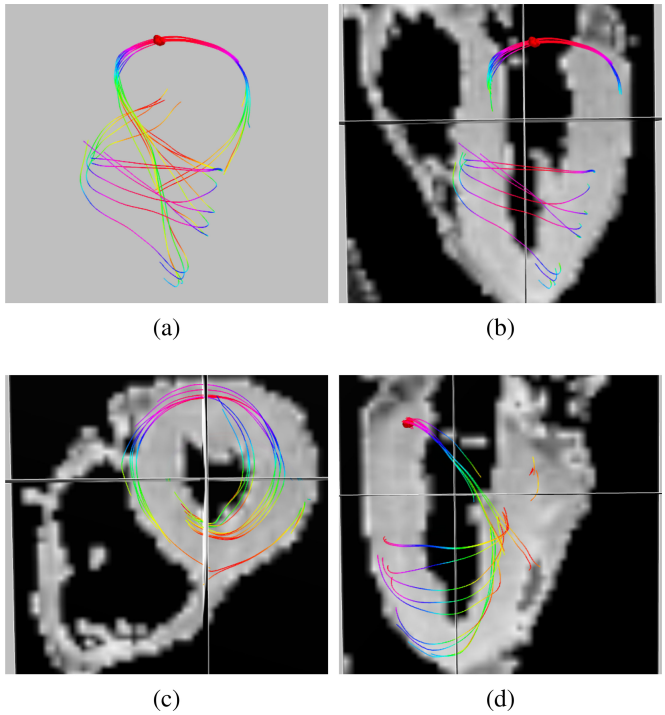


Fig. 13. Ten cardiac fibers with no apparent helical structure. (The red points are the reference points used for unfolding.)

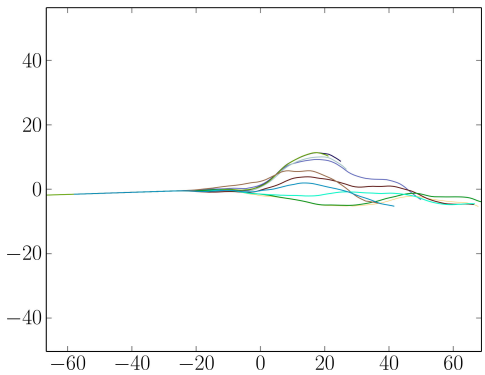


Fig. 14. Embedding of the fibers shown in Fig. 13. (Axis units are mm.)

and the negligible FD values are in agreement with the band-like organization of the 3-D fibers.

*2) Complex Fiber Configuration:* The architecture of the set of fibers displayed in Fig. 11 is more difficult to apprehend than that of the fibers in Fig. 9. The corresponding embedding is shown in Fig. 12. We observe that the unfolded fibers do not scatter as much as may be erroneously inferred from the 3-D representations. Together with the short-axis view in Fig. 11(c), unfolding reveals that the selected fibers are consistent with the helical band model. The EA (about 54%) is smaller than in the previous example (see Table V); this indicates that the fibers in Fig. 11 are less close to a 2-D manifold than those in Fig. 9. The FD remains negligible (below 0.5%), revealing that the set of 3-D fibers also has a band-like structure. This latter observation is noteworthy, for the band-like organization is hardly visible from 3-D rendering.

*3) Fibers With No Apparent Helical Structure:* An even more complicated example is shown in Fig. 13. The ten selected fibers are sampled with a step-length equal to the voxel-size; they are close to each other along one third of their length, and they scatter along the apex-base axis. Although a spiral shape is clearly visible from Fig. 13(c), the 3-D representations do not allow us to conclude that the fibers have an helical structure. Fig. 14 shows the embedding produced by unfolding. The EA is 85.4%, which confirms that the underlying dimensionality of the fibers is two. The FD (about 1.1%) is larger than in the two previous examples, but the fibers tend to regroup after moving away from each other. Therefore, the band model is acceptable to the extent that fibers can scatter within the helical structure. Fig. 15 shows the embedding of middle segments of the four longest fibers. The associated accuracy is 98.9%, and so these fiber segments lie on a 2-D manifold even though they move away from each other in the apex region. This confirms

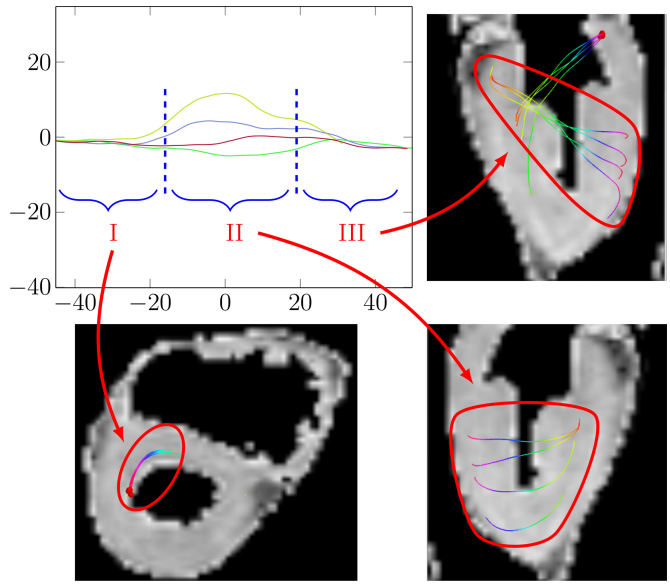


Fig. 15. Embedding of fiber segments from Fig. 13. The unfolded fiber segments can be divided into three parts: (I) they follow approximately the same trajectory, (II) then they move away from each other in the apex region, and (III) they finally regroup.

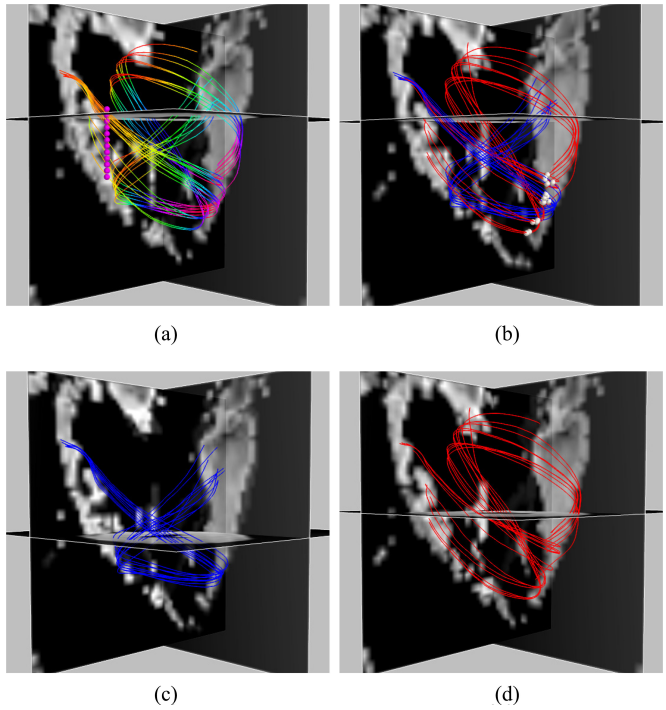


Fig. 16. Eighteen cardiac fibers separated into two groups with different organizations: (a) the fibers pass through the vertically aligned points displayed in pink; (b) the reference points used for embedding are displayed in white (they are the closest points to a user-defined vertical plane); (c), (d) the two groups of nine fibers each do not seem to lie near a same manifold.

again that the specific structure of the cardiac fibers is more completely assessed by combining information from both 3-D rendering and 2-D embedding.

*4) Fiber Groups With Different Organizations:* We conclude our experiments by further examining the effect of the neighborhood-size parameter $k$. Fig. 16 shows eighteen fibers passing through vertically aligned points [displayed in pink in Fig. 16(a)] in the epicardium. These fibers were separated into two groups of nine fibers each according to their shape. The separate 3-D renderings of these groups in Figs. 16(c) and (d) do not allow us to conclude whether they lie near a same manifold. Fig. 17 shows the unfolding results obtained for values of $k$ ranging from 10 to 35 [we used the reference points displayed in white in Fig. 16(b)]. The spectra of the corresponding Gram matrices are displayed in Fig. 18 in the form of cumulative bar charts. Both representations show an abrupt change for a value of $k$ between 20 and 25. More precisely, the break occurs for $k = 24$, which is the value above which the local isometry constraints involve at least nine fibers on average. The similar embeddings and the spectra obtained for $k \geqslant 24$ indicate two things: First, the two groups of fibers lie near a same manifold; second, the critical value of $k$ is that which creates attachment between the two groups. These observations suggest that $k$ can be set automatically by unfolding with increasing neighborhood size until an abrupt increase of the ratio $\lambda_1/\lambda_2$ (or, equivalently, an abrupt decrease in FD) occurs.

## IV. Discussion and Conclusion

We introduced an original approach to assess the architecture of the human heart—the unfolding of cardiac fibers under local isometry constraints using SDP. This new tool facilitates the analysis of complex 3-D fiber structures, it allows quantitative measurements of fiber organization via the eigenvalues of the Gram matrices defining the embeddings, and it provides fiber grouping information.

Our unfolding algorithm is controlled by

1) the set of reference points involved in the definition of the distance $d_{\mathbf{X}}$ (see Section II-D), and
2) the neighborhood-size parameter $k$ that controls the local isometry constraints (see Section II-E).

It is best practice to take the reference points in a narrow region intersected by all the fibers to unfold, if such exists. However, although the reference points affect the adjacency matrix, fiber unfolding is weakly sensitive to the choice of the reference region because it preserves local Euclidean distances rather than $d_{\mathbf{X}}$. The effect of the parameter $k$ is more critical. If it is too small (that is, if the neighborhoods $\mathcal{N}_k(\mathbf{x}_m)$ do not involve enough fibers), then too much structure information is lost in the unfolding process, and this results in faulty embeddings such as those displayed in Figs. 17(a)–(c). Increasing $k$ strengthens and widens the local isometry constraints, which makes it more difficult to embed fiber sets with complex organization but preserves structures. In practice, $k$ can be determined by considering increasing values until a drop in FD is observed, as illustrated by the Gram matrix spectra in Fig. 18. We suggest to start with $k = 15$, which generally produces good embeddings, and then increase it by increments of 3 if necessary.

Our experiments show that 2-D embedding is an interesting supplement to 3-D cardiac fiber rendering. In particular, it reveals specific fiber propagation patterns such as band-like

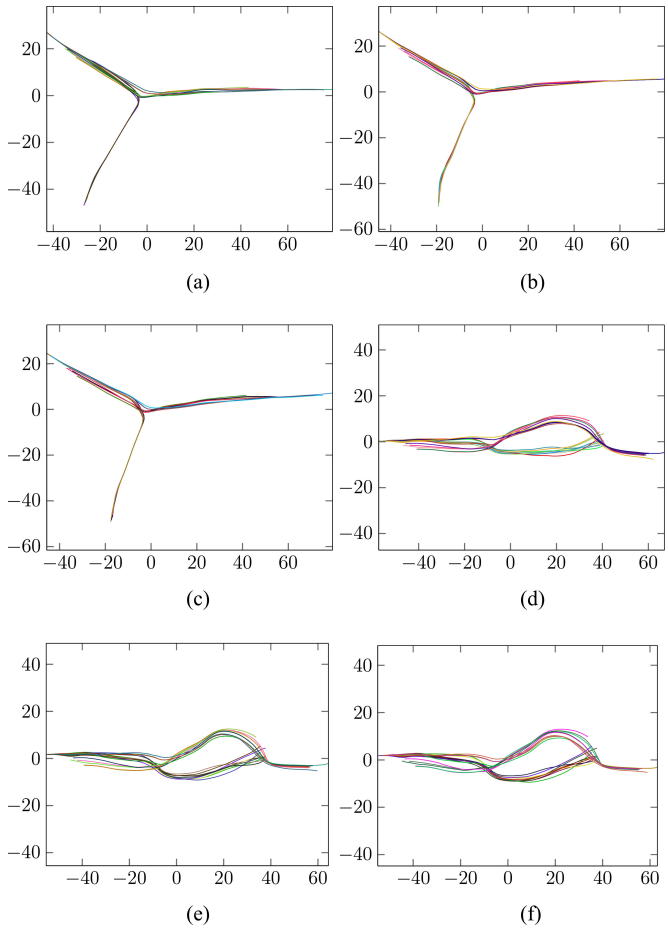


Fig. 17. Embeddings of the fibers in Fig. 16 obtained with different values of $k$. (Axis units are mm.)

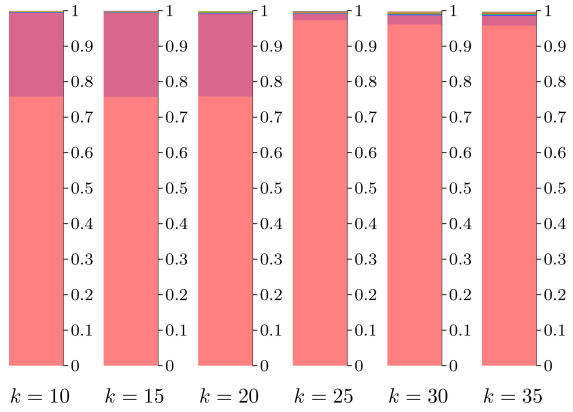


Fig. 18. Cumulative bar charts of the spectra of the Gram matrices associated with the embeddings shown in Fig. 17.

organization (as for the fiber sets displayed in Figs. 9, 11 and 16) and scattering in the vicinity of the apex (as for the fibers displayed in Fig. 13). This information could be used for better understanding laminar fiber architecture [17], [36], [37], for performing fiber clustering [25], [28], and for distinguishing abnormal from healthy hearts [20], [38]–[40].

## ACKNOWLEDGMENT

The authors would like to thank Dr. L. Fanton and P. Croisille for data acquisition.

## REFERENCES

[1] L. Krehl, *Beitrge Zur Kenntniss Der Fllung Und Entleerung Des Herzens.* Leipzig, Germany: Hirzel, 1891.
[2] J. MacCallum, "On the muscular architecture and growth of the ventricles of the heart," *Johns Hopkins Hosp. Rep.*, vol. 9, pp. 307–335, 1900.
[3] F. Mall, "On the muscular architecture of the ventricles of the human heart," *Am. J. Anat.*, vol. 11, no. 3, pp. 211–266, 1911.
[4] J. Robb and R. Robb, "The normal heart: Anatomy and physiology of the structural units," *Amer. Heart J.*, vol. 23, no. 4, pp. 455–467, 1942.
[5] R. Rushmer, D. Crystal, and C. Wagner, "The functional anatomy of ventricular contraction," *Circ. Res.*, vol. 1, no. 2, pp. 162–170, 1953.
[6] F. Torrent-Guasp, "Organizacion de la musculatura cardiaca ventricular," in *El Fallo Mecànico del Corazon*. Barcelona, Spain: Toray, 1975, pp. 3–36.
[7] D. Streeter, "Gross morphology and fiber geometry of the heart," in *Handbook of Physiology*. Bethesda, MD, USA: Amer. Physiol. Soc., 1979, pp. 61–112.
[8] R. Greenbaum, S. Ho, D. Gibson, A. Becker, and R. Anderson, "Left ventricular fibre architecture in man," *Br. Heart J.*, vol. 45, no. 3, pp. 248–263, 1981.
[9] P.-S. Jouk, Y. Usson, G. Michalowicz, and F. Parazza, "Mapping of the orientation of myocardial cells by means of polarized light and confocal scanning laser microscopy," *Microsc. Res. Tech.*, vol. 30, no. 6, pp. 480–490, 1995.
[10] D. Sanchez-Quintana, V. Garcia-Martinez, V. Climent, and J. Hurle, "Morphological changes in the normal pattern of ventricular myoarchitecture in the developing human heart," *Anat. Rec.*, vol. 243, no. 4, pp. 483–495, 1995.
[11] P. Lunkenheimer, K. Redmann, H. Scheld, K.-H. Dietl, C. Cryer, K.-D. Richter, J. Merker, and W. Whimster, "The heart muscle's putative secondary structure: Functional implications of a band-like anisotropy," *Technol. Health Care*, vol. 5, no. 1, pp. 53–64, 1997.
[12] B. Taccardi, E. Macchi, R. Lux, P. Ershler, S. Spaggiari, S. Baru, and Y. Vyhmeister, "Effect of myocardial fiber direction on epicardial potentials," *Circulation*, vol. 90, no. 6, pp. 3076–3090, 1994.
[13] C.-Y. Chung, H. Bien, and E. Entcheva, "The role of cardiac tissue alignment in modulating electrical function," *J. Cardiovasc. Electrophysiol.*, vol. 18, no. 12, pp. 1323–1329, 2007.
[14] P. Basser, J. Mattiello, and D. LeBihan, "Estimation of the effective self-diffusion tensor from the NMR spin echo," *J. Magn. Reson. B*, vol. 103, no. 3, pp. 247–254, 1994.
[15] E. Piuze, J. Sporring, and K. Siddiqi, "Moving frames for heart fiber geometry," in *Information Processing in Medical Imaging*. New York, NY, USA: Springer, 2013, pp. 524–535.
[16] P. Savadjiev, G. Strijkers, A. Bakermans, E. Piuze, S. Zucker, and K. Siddiqi, "Heart wall myofibers are arranged in minimal surfaces to optimize organ function," *Proc. Nat. Acad. Sci. U.S.A.*, vol. 109, no. 24, pp. 9248–9253, 2012.
[17] D. Rohmer, A. Sitek, and G. Gullberg, "Reconstruction and visualization of fiber and laminar structure in the normal human heart from ex vivo diffusion tensor magnetic resonance imaging (DTMRI) data," *Invest. Radiol.*, vol. 42, no. 11, pp. 777–789, 2007.
[18] C. Frindel, M. Robini, and Y. Zhu, "A graph-based approach for automatic cardiac tractography," *Magn. Reson. Med.*, vol. 64, no. 4, pp. 1215–1229, 2010.
[19] F. Yang, Y. Zhu, I. Magnin, J. Luo, P. Croisille, and P. Kingsley, "Feature-based interpolation of diffusion tensor fields and application to human cardiac DT-MRI," *Med. Image Anal.*, vol. 16, no. 2, pp. 459–481, 2012.
[20] H. Lombaert, J.-M. Peyrat, P. Croisille, S. Rapacchi, L. Fanton, F. Cheriet, P. Clarysse, I. Magnin, H. Delingette, and N. Ayache, "Human atlas of the cardiac fiber architecture: Study on a healthy population," *IEEE Trans. Med. Imag.*, vol. 31, no. 7, pp. 1436–1447, Jul. 2012.
[21] N. Toussaint, C. Stoeck, T. Schaeffter, S. Kozerke, M. Sermesant, and P. Batchelor, "*In vivo* human cardiac fibre architecture estimation using shape-based diffusion tensor processing," *Med. Image Anal.*, vol. 17, no. 8, pp. 1243–1255, 2013.
[22] L. Zhukov and A. Barr, "Heart-muscle fiber reconstruction from diffusion tensor MRI," in *Proc. 14th IEEE Vis. Conf.*, 2003, pp. 597–602.

[23] M. Kocica, A. Corno, F. Carreras-Costa, M. Ballester-Rodes, M. Moghbel, C. Cueva, V. Lackovic, V. Kanjuh, and F. Torrent-Guasp, "The helical ventricular myocardial band: Global, three-dimensional, functional architecture of the ventricular myocardium," *Eur. J. Cardiothorac. Surg.*, vol. 29, pp. S21–40, 2006.

[24] H. Wei, M. Viallon, B. Delattre, L. Wang, V. Pai, H. Wen, H. Xue, C. Guetter, P. Croisille, and Y. Zhu, "Assessment of cardiac motion effects on the fiber architecture of the human heart *in vivo*," *IEEE Trans. Med. Imag.*, vol. 32, no. 10, pp. 1–11, Oct. 2013.

[25] C. Frindel, M. Robini, and Y. Zhu, "Cardiac fibre trace clustering for the interpretation of the human heart architecture," in *Functional Imaging and Modeling of the Heart*. New York, NY, USA: Springer, 2009, pp. 39–48.

[26] P. Batchelor, F. Calamante, J.-D. Tournier, D. Atkinson, D. Hill, and A. Connelly, "Quantification of the shape of fiber tracts," *Magn. Reson. Med.*, vol. 55, no. 4, pp. 894–903, 2006.

[27] A. Leemans, J. Sijbers, S. De Backer, E. Vandervliet, and P. Parizel, "Multiscale white matter fiber tract coregistration: A new feature-based approach to align diffusion tensor data," *Magn. Reson. Med.*, vol. 55, no. 6, pp. 1414–1423, 2006.

[28] L. O'Donnell, M. Kubicki, M. Shenton, M. Dreusicke, W. Grimson, and C. Westin, "A method for clustering white matter fiber tracts," *Amer. J. Neuroradiol.*, vol. 27, no. 5, pp. 1032–1036, 2006.

[29] S. Zhang, S. Correia, and D. Laidlaw, "Identifying white-matter fiber bundles in DTI data using an automated proximity-based fiber clustering method," *IEEE Trans. Vis. Comput. Graphics*, vol. 14, no. 5, pp. 1044–1053, Sep./Oct. 2008.

[30] L. Cayton, "Algorithms for manifold learning," Univ. California, San Diego, CA, USA, Tech. Rep. CS2008-0923, 2005.

[31] L. van der Maaten, E. Postma, and H. van den Herik, "Dimensionality reduction: A comparative review," Tilburg Univ., Tilburg, The Netherlands, Tech. Rep. 2009-005, 2009.

[32] K. Weinberger and L. Saul, "Unsupervised learning of image manifolds by semidefinite programming," in *Proc. IEEE Comput. Soc. Conf. Comput. Vis. Pattern Recognit.*, 2004, pp. 988–995.

[33] L. Vandenberghe and S. Boyd, "Semidefinite programming," *SIAM Rev.*, vol. 38, no. 1, pp. 49–95, 1996.

[34] H. Li, M. Robini, F. Yang, and Y. Zhu, "A neighborhood-based probabilistic approach for fiber tracking in human cardiac DTI," in *Proc. IEEE Int. Symp. Biomed. Imag.*, 2012, pp. 9–13.

[35] B. Borchers, "CSDP: A C library for semidefinite programming," *Optim. Methods Softw.*, vol. 11, no. 1–4, pp. 613–623, 1999.

[36] I. LeGrice, B. Smaill, L. Chai, S. Edgar, J. Gavin, and P. Hunter, "Laminar structure of the heart: ventricular myocyte arrangement and connective tissue architecture in the dog," *Amer. J. Physiol. Heart Circ. Physiol.*, vol. 269, no. 2, pp. H571–582, 1995.

[37] K. Costa, Y. Takayama, A. McCulloch, and J. Covell, "Laminar fiber architecture and three-dimensional systolic mechanics in canine ventricular myocardium," *Amer. J. Physiol. Heart Circ. Physiol.*, vol. 276, no. 2, pp. H595–607, 1999.

[38] M. Wu, W. Tseng, M. Su, C. Liu, K. Chiou, V. Wedeen, T. Reese, and C. Yang, "Diffusion tensor magnetic resonance imaging mapping the fiber architecture remodeling in human myocardium after infarction correlation with viability and wall motion," *Circulation*, vol. 114, no. 10, pp. 1036–1045, 2006.

[39] W. Tseng, J. Dou, T. Reese, and V. Wedeen, "Imaging myocardial fiber disarray and intramural strain hypokinesis in hypertrophic cardiomyopathy with MRI," *J. Magn. Reson. Imag.*, vol. 23, no. 1, pp. 1–8, 2006.

[40] M. Wu, M. Su, Y. Huang, K. Chiou, P. Yang, H. Pan, T. Reese, V. Wedeen, and W. Tseng "Sequential changes of myocardial microstructure in patients postmyocardial infarction by diffusion-tensor cardiac MR: Correlation with left ventricular structure and function," *Circ. Cardiovasc. Imag.*, vol. 2, no. 1, pp. 32–40, 2009.

Authors' photographs and biographies not available at the time of publication.